This is the accepted manuscript made available via CHORUS. The article has been published as:

Tunable atomically enhanced moiré Berry curvatures in twisted triple bilayer graphene

Konstantin Davydov, Ziyan Zhu, Noah Friedman, Ethan Gramowski, Yaotian Li, Jack Tavakley, Kenji Watanabe, Takashi Taniguchi, Mitchell Luskin, Efthimios Kaxiras, and Ke Wang

Phys. Rev. B **111**, L161120 — Published 23 April 2025

DOI: 10.1103/PhysRevB.111.L161120

Tunable Atomically Enhanced Moiré Berry Curvatures in Twisted Triple Bilayer Graphene

Konstantin Davydov[1], Ziyan Zhu[2], Noah Friedman[1], Ethan Gramowski[1], Yaotian Li[1], Jack Tavakley[1], Kenji Watanabe[3], Takashi Taniguchi[4], Mitchell Luskin[5], Efthimios Kaxiras[6,7], Ke Wang[1*]

[1]*School of Physics and Astronomy, University of Minnesota, Minneapolis, Minnesota 55455, USA*
[2]*Stanford Institute for Materials and Energy Sciences, SLAC National Accelerator Laboratory, Menlo Park, CA 94025, USA*
[3] *Research Center for Electronic and Optical Materials, National Institute for Materials Science, 1-1 Namiki, Tsukuba 305-0044, Japan*
[4] *Research Center for Materials Nanoarchitectonics, National Institute for Materials Science, 1-1 Namiki, Tsukuba 305-0044, Japan*
[5]*School of Mathematics, University of Minnesota, Minneapolis, Minnesota 55455, USA*
[6]*Department of Physics, Harvard University, Cambridge, Massachusetts 02138, USA*
[7]*John A. Paulson School of Engineering and Applied Sciences, Harvard University, Cambridge, Massachusetts 02138*
**Corresponding author. Email: kewang@umn.edu*

We report a twisted triple bilayer graphene platform consisting of three units of Bernal bilayer graphene (BLG) consecutively twisted at 1.49° and 1.68°. We demonstrate the atomic reconstruction between the two competing moiré superlattices strongly enhances the Berry curvature of each moiré band insulator state, characterized by measured strong nonlocal valley Hall effect (VHE) that sensitively depends on the inter-moiré competition strength, tunable by manipulating the out-of-the-plane carrier distribution. Our study sheds new light on the microscopic mechanism of atomic and electronic reconstruction in twisted multilayer systems, by systematically investigating transport signatures of moiré Berry curvature and its enhancement from moiré-of-moiré lattice reconstruction. We show that the reconstructed electronic band can be versatilely tuned by electrostatics, providing an approach toward engineering the band structure and its topology for a novel quantum material platform with designer electrical and optical properties.

The interference between two slightly rotated atomic lattices, which occurs at the homo and heterointerface of atomically thin materials stacked with small twist angles, gives rise to a moiré superlattice and flat bands where electronic interactions are enhanced. Novel material properties have been reported in such structures, including ferromagnetism [1], the quantum anomalous Hall effect [2–5], quantum spin Hall effect [6], Mott insulators [7–9] and superconductivity [10,11].

Beyond twisted bilayers, the addition of a third 2D layer further enriches the emergent physics [12]. When the third layer aligns with the first layer, the original moiré superlattice is atomically stabilized with enhanced correlated insulator and superconducting states [13–15]. When the third layer is misaligned with the existing layers, two separate moiré superlattices coexist [16–19]. The beating between the two moiré superlattices gives rise to higher order superlattices [20,21], referred to as moiré-of-moiré (MoM) superlattices. A wide range of competing length scales coexist, giving rise to an abundance of new electronic properties [22–24], including an inter-moiré Hofstadter butterfly [19], quasicrystal states [17], correlated charge density wave insulators [23] and signatures of correlated insulating and superconducting states at an extremely low carrier density (~ 10^{10} cm^{-2}) [25].

To understand how competing atomic structures alter the resulting electronic band in a moiré-of-moiré superlattice, we fabricated a twisted triple bilayer graphene (tTBLG) device consisting of three units of Bernal bilayer graphene (BLG) consecutively twisted at 1.49° and 1.68° [see Fig. 1(a) and Supplemental Material [26]: Section S1]. The choice of different twist angles ensures that the sizes of two coexisting moiré superlattices are sufficiently different [Figs. 1(b)–1(c)], so that the transport signatures from each moiré lattice can be isolated and traced back to insulator states at different carrier densities, and the interaction between the moiré superlattices can be examined via emergent higher order transport features at the carrier density in between full fillings of the two individual moiré patterns. The choice of BLG as the basic unit of stacking allows for characterization of atomically induced band reconstruction by tracking the Berry curvature [27,28]. Berry curvature hot spots were previously reported at the band edges of a parabolic like band [at the charge neutrality point (CNP) of BLG or band insulator states of a moiré lattice] [29–34], and can be sensitively enhanced by atomic strain/reconstruction from aligned hBN that further breaks the inversion symmetry [33,35–38].

Figure 1(d) shows the calculated band structure of tTBLG at the twist angles of 1.49° and 1.68°. The low energy bands are parabolic instead of linear as in twisted bilayer or trilayer graphene, with the potential of hosting a Berry curvature hot spot at the band edges of moiré and MoM bands. Figure 1(e) shows the measured under applied top, V_{TG}, and back gate voltages, V_{BG}, four-probe longitudinal local resistance $R_L = R_{xx}$ (Region 1 of the tTBLG device, between Contacts 4 and 3) as a function of the applied displacement field D (having the positive direction toward

the graphite gate), and carrier density n (see Supplemental Material [26]: Section S2 for D and n calculations). The top (bottom) axis is given in terms of filling factors for top (bottom) moiré superlattices $\nu_T = 4n/n_T$ ($\nu_B = 4n/n_B$), where n_T (n_B) correspond to 4 charge carriers per top (bottom) moiré unit cell. Signature fillings from the top (bottom) moiré patterns are highlighted by yellow (purple) lines, where local resistance peaks are expected at integer fillings, including band insulator states at full fillings (solid lines), and correlated insulator states at half fillings (dashed lines) [23].

At $\nu_T = -4(+4)$, the hole-type (electron-type) charge carries are localized in the top moiré superlattice by a positive (negative) D. The tTBLG in its entirety therefore exhibits insulating behavior, confirmed by the temperature dependence [Fig. 3(a), see also Supplemental Material [26]: Section S4], with an estimated thermal activation gap of ~6 meV for $\nu_T = 4$ and ~3 meV for $\nu_T = -4$, respectively.

In tTBLG, we show that the coexistence of two moiré superlattices and their interaction further enhances the Berry curvature of the moiré band insulator states, and can be sensitively manipulated by tuning the inter-moiré interaction strength. The Berry curvature is characterized with the well-established "nonlocal" measurement at $B = 0$ T [30–41]. The valley-specific anomalous velocity drives the ballistic carrier trajectory astray (more so than conventional current diffusion [28,30–38,40,41]), resulting in its detection at voltage probes sufficiently away from the current path.

We apply current I_{73} between Contact 7 and 3 of the tTBLG device [Figs. 1(b) and 2(a)], and measure voltage V_{64} between Contact 6 and 4 (as a result of transverse valley-polarized current) away from the current excitation (nonlocal) to study valley Hall effect (VHE) [30–38,40–43]. The nonlocal resistance $R_{NL} = V_{64}/I_{73}$ as a function of the carrier density and D field is plotted in Fig. 2(b). Nonlocal resistance peaks are found near $\nu_T = \pm 4$ and $D < 0$ ($D > 0$), satisfying prerequisites for observing moiré Berry curvature hot spot: (1) Fermi level is near the edge of the band insulator gap, (2) the bottom BLG is depleted of charge carriers (and thus does not contribute to the transport). When both conditions are met, the tTBLG overall is insulating with its Berry curvature well-defined. Near the Berry curvature hotspot, the interlayer screening is negligible, and the displacement field can be approximated as uniform across all 3 layers. Similarly, a nonlocal resistance peak is found near $\nu_B = +4$ and $D > 0$, near the band insulator gap of the bottom moiré while the top BLG is depleted of electron-type carriers. Additionally, substantial nonlocal resistance is observed at CNP at $D > 0$, arising from Berry curvature hot spot near displacement-field-induced BLG bandgap [30,31], when all three BLG layers are depleted of charge carriers. The absence of an expected nonlocal resistance peak near $\nu_B = -4$, and CNP at $D < 0$ can be explained by (1) broken electron-hole symmetry in tTBLG; (2) top BLG is not in-gap for $D < 0$ (consistent with a smaller measured R_{xx}) making such states less insulating or out of the measurement range.

These resistance peaks arise from the ballistic valley current driven by the Berry curvature, instead of stray currents due to diffusive Ohmic transport, supported by several separate experimental observations. First, the longitudinal resistance peaks [Fig. 1(e)] corresponding to the correlated insulator states are completely absent in the nonlocal measurement [Fig. 2(b)], confirming the origin of nonlocal resistance peaks as curved ballistic transport due to the Berry curvature, instead of a simple diffusive transport at resistive insulating states. Moreover, following previously-established methods [30–32,34,35,38], we measure the nonlocal signal R_{NL} at voltage probes with varying distance L to the applied current (see Supplemental Material [26]: Section S7). The R_{NL} as a function of L is fitted by $\exp(-L/\xi)$, giving a decay length $\xi = 4\pm2$ μm, a change much slower than the decay due to diffusive Ohmic transport, and consistent with the inter-valley scattering length.

In addition, the trivial Ohmic contribution (R_{NLO}) from the stray currents can be estimated from the measured local ($R_L = R_{xx}$) resistance by $R_{NLO} = R_L(w/L)\exp(-L/\lambda)$, where $\lambda = w/\pi$; $w = 0.9$ μm, $L = 1.6$ μm are the width and length of the channel. Following previously well-established methods [30–32,34,35,38], the estimated Ohmic contribution can then be compared to the measured nonlocal resistance to understand the origin of measured R_{NL}. As an example [Fig. 2(c)], at $\nu_T = -4$ and $D/\varepsilon_0 = +0.45$ V/nm, the measured nonlocal resistance R_{NL} [scanned across white line denoted in Fig. 2(b)] is over 100 times larger than expected contribution from the diffusive Ohmic transport R_{NLO} (see Supplemental Material [26]: Section S3 for other band insulator states). The Ohmic contribution is therefore marginal, and the nonlocal resistance is primarily attributed to the Berry curvature.

Last but not least, the power law scaling between the measured local and nonlocal resistances $R_{NL} \sim R_L^{\gamma}$ have been previously used to determine the nature of the nonlocal signal [30–35,37,38,41,42]. Ohmic behavior is linear in nature ($\gamma = 1$), while nonlocal signal caused by the Berry curvature is expected to be nonlinear, with either $\gamma > 1$ or $\gamma < 1$ depending on the saturation of ballistic valley current channel [42]. In contrast to the previously reported Berry curvature hot spot in BLG, tBLG and tDBLG [30–34,38], the moiré Berry curvature hot spot in tTBLG shows an abrupt change across the band insulator gap. To show this, the measured nonlocal resistance near $\nu_T = -4$ [Fig. 2(c)] is categorized into electron-type (blue) and hole-type (red). The R_{NL} versus R_L [Fig. 2(d)] is then separately plotted for each category of carrier type, and individually fitted against $R_{NL} \sim R_L^{\gamma}$. Both show a good fit to a nonlinear power law dependence, suggesting a Berry curvature hot spot as the underlying mechanism. The quantitative difference in the extracted power γ suggests that the Berry curvature hot spot shows a strong electron-hole asymmetry near $\nu_T = -4$, with

the Berry curvature hot spot being stronger near the electron-type band edges of the $\nu_T = -4$, leading to a stronger valley Hall current [Fig. 2(e), solid arrows] saturating the maximum current capacity of ballistic conductance channels with $\gamma < 1$. The reverse effect, weaker Berry curvature hot spot and valley Hall current, correspond to hole-type band edges, with $\gamma > 1$ [see Fig. 2(e), hollow black arrows] [42].

We show that the observed strong Berry curvature hot spot at $\nu_T = -4$ of the top moiré pattern is enhanced by the atomic reconstruction and electronic modification with the bottom moiré pattern, which further breaks the inversion symmetry and alters the band curvature. This can be demonstrated by measuring the power law γ [Fig. 2(f)], while tuning the strength of inter-moiré interaction with D [19]. As the D field increases, the electron-type carrier is less localized in the top moiré pattern while its interaction with bottom moiré is enhanced leading to $\nu_T = -4$ band insulator gaps whose Berry curvature is strongly reinforced by the presence of the bottom moiré pattern (the reverse effect corresponds to decreasing D field, with more localized carriers in the top moiré pattern and suppressed interaction with the bottom moiré pattern). As a result, the power law γ is observed to be continuously tunable by the field value (D) over one order of magnitude. At small D, when the inter-moiré interaction is weakest, the power law $\gamma = 3$ is similar to the previously reported valley Hall effect without an atomic reconstruction from aligned hBN [33,35,37,38]. At large D, when the inter-moiré enhancement is strongest, the record-low $\gamma = 0.5$ suggests an unusually large valley Hall current driven by an extraordinarily-strong Berry curvature, oversaturating the available ballistic channels, more so than atomically-enhanced valley Hall effect previously reported in hBN-aligned systems [35,37,38]. The displacement field dependence is also consistent with the Berry curvature hotspot belonging to band insulator states of top moiré superlattice instead of the bottom bilayer graphene, with the latter characterized to yield weaker valley Hall signal at charge neutrality point n=0.

In contrast, $\gamma = 3$ is observed for the hole-type carriers near $\nu_T = -4$, largely regardless of the D field applied. This suggests that the inter-moiré atomic reconstruction has much weaker implication to the hole-like band edges, possibly due to a large electron-hole asymmetry in band dispersion or different ground state atomic orbitals for electrons and holes.

To extract the characteristic energy scale of the moiré Berry curvature hot spot and to further confirm their microscopic physics pictures, we measure the temperature dependence (Figure 3) of the non-local transport. Figure 3(a) plots the measured local resistance at the peak (black) and half peak (red: hole-like carriers; blue: electron-like carriers) as a function of temperature. At temperatures $T > 10$ K, the charge carriers across the $\nu_T = -4$ band insulator gap are thermally activated, resulting in a measured local resistance that decreases with increasing temperature. By fitting the temperature dependence at $T > 10$ K with the Arrhenius law: $R_L \sim \exp\left(\frac{\Delta_L}{2k_B T}\right)$ [Fig. 3(b), dashed], the size of band-insulator gap is extracted to be on the order of meV [Fig. 4(b), diamonds], consistent with calculated band structure. The temperature dependences of the peak (black) and half-peak (red, blue) local resistance [Figs. 3(a)–3(b)] give similar band gap sizes [Fig. 4(b), diamonds with the respective colors], indicating thermal activation of carriers at partial filling of the conductance and valence band edges near $\nu_T = -4$.

The nonlocal resistance R_{NL} near Berry curvature hot spot at $\nu_T = -4$ is also measured at varying temperature [Fig. 3(c)], from 10 mK to 20 K with an equal step size of $\Delta T \sim 2$ K. The resistance peak shows a weak temperature dependence below 10 K (with the curves for $T < 10$ K largely overlapping with each other), while drastically diminishes as T rises above 10 K. The change in temperature dependence can be seen more evidently when plotting R_{NL} as a function of temperature [Fig. 3(d)], measured at the peak (black) and half-height on the hole-like (red) and electron-like (blue). The three sets of data all exhibit a strong (weak) T-dependence above (below) $T \sim 10$ K, with fitting to $\exp\left(\frac{\Delta_{NL}}{2k_B T}\right)$ above 10 K yielding a similar thermal activation gap Δ_{NL}. This is consistent with the nonlocal signal (peak or half-height) being expected only when the Fermi level is near mid gap or at the band edges of the band insulator states. The displacement field dependence of the extracted Δ_{NL} [Fig. 4(b), triangles] is also consistent with that of γ [Fig. 2(f)], with a larger Δ_{NL} being observed at higher D fields when stronger inter-moiré interaction further enhances the Berry curvature hot spot.

At all values of the D field, Δ_{NL} is consistently larger than the thermal activation gaps Δ_L at $\nu_T = -4$ [Fig. 4(b)]. The two energy scales near the band insulator states are illustrated in Fig. 4(a), each determining different aspects of the transport behavior near the Berry curvature hot spot: (1) the band insulator gap $\Delta_L = E_e - E_h$, defined as the difference between electron-like band minima E_e and hole-like band maxima E_h, the conventional definition of a band gap; this gap determines the conventional transport such as R_{xx}. (2) The nonlocal gap $\Delta_{NL} = E_e^* - E_h^*$, defined as the difference between the E_e^* and E_h^*, the energy in electron-like and hole-like bands, beyond which ($E > E_e^*$ and $E < E_h^*$) the Berry curvature becomes zero. This gap affects the anomalous transport aided by Berry curvature, such as R_{NL}.

The observed temperature dependence is consistent in each case with the Berry curvature hot spot at $\nu_T = -4$, with a $\Delta_L = 3$ meV and $\Delta_{NL} = 10$-15 meV. At temperature below 10 K (or $\Delta_{NL}/10$), additional carriers may be thermally excited across Δ_L, but they reside at band edges well within the Berry curvature hot spot (between E_e^* and E_h^*), equally capable of carrying valley Hall current that saturates the ballistic conductance channel. At temperature above 10 K (or $\sim \Delta_{NL}/10$), a significant portion of the carriers in the applied current start to fall energetically outside the Berry

curvature hot spot, and thus stop experiencing the anomalous velocity, no longer contributing to the nonlocal signal, hence the change of temperature dependence [Figs. 3(c)–3(d)] of R_{NL} at $T \sim 10$ K, and a significantly larger Δ_{NL} [Fig. 4(b)] that more sensitively depends on the D field applied compared to Δ_L. This implies that the enhancement of the Berry curvature hot spot (characterized by Δ_{NL}) is more attributed to the inter-moiré interaction than the evolution of the band structure itself (characterized by Δ_L).

Figure 4(c) presents a log-log plot of R_{NL} vs R_L where each data point is taken at a different temperature T. Following the previously-established approaches [31–34], we observe distinct power law behaviors at temperature range above and below $T \sim 10$ K, consistent with our physics picture [Fig 4(a)]. At low temperature range below $T \sim 10$ K [top left part of Fig. 4(c), R_{NL} remains constant while R_L is rapidly decreasing with T (with power law $\gamma < 0.5$)]. In this regime, the ballistic valley conduction channel is saturated, and thermally activated additional carriers are capable of contributing to local transport only. This behavior persists up to critical temperatures of $T_0 \sim 5$ K ($T_0 \sim 8$ K) for the hole- (electron-) like carriers and up to $T_0 \sim 7$ K for the resistance peak, consistent with the larger Berry curvature hot spot at electron side. At higher temperature ($T > 10$ K), charge carriers are thermally excited away from the Berry curvature hot spot near band edges. The weaker Berry curvature they experience makes the ballistic valley conducting channel unsaturated, resulting in an observed power law of $\gamma \sim 3$-4 for both charge carrier types [Fig. 4(c)]. This is consistent with the ratio of the previously extracted characteristic energy scales Δ_{NL}, Δ_L [Fig. 4(b)] and the theoretical values [42] of γ for an unsaturated valley conductance channel.

In conclusion, we studied a twisted triple bilayer graphene device with consecutive twist angles of 1.49° and 1.68°, in which atomic and electronic reconstruction between two coexisting moiré superlattices gives rise to significantly enhanced moiré Berry curvature hot spots. The latter result in amplified valley currents near moiré band insulator states, characterized by measured strong nonlocal valley Hall effect, which depends sensitively on electrostatically tuned inter-moiré competition strength, supporting several orthogonal sets of experimental observations. Our study sheds new light on the microscopic nature of atomic and electronic properties stemming from the interplay and competition of moiré superlattices, providing an approach toward engineering the band structure and its topology for a novel quantum material platform with designer electrical and optical properties.

We thank Andrey Chubukov and Boris Shklovskii for useful discussions. This work was supported by NSF DMREF Award 1922165. Z.Z. is supported by a Stanford Science Fellowship. E.K. acknowledges support from Simons Foundation Award no. 896626. Nanofabrication was conducted in the Minnesota Nano Center, which is supported by the National Science Foundation through the National Nanotechnology Coordinated Infrastructure (NNCI) under Award Number ECCS-2025124. Portions of the hexagonal boron nitride material used in this work were provided by K.Wat. and T. T. K.Wat. and T.T. acknowledge support from the JSPS KAKENHI (Grant Numbers 20H00354, 21H05233 and 23H02052) and World Premier International Research Center Initiative (WPI), MEXT, Japan

The supporting data for this article are openly available from the Zenodo archive [44].

*kewang@umn.edu

[1] A. L. Sharpe, E. J. Fox, A. W. Barnard, J. Finney, K. Watanabe, T. Taniguchi, M. A. Kastner, and D. Goldhaber-Gordon, Emergent ferromagnetism near three-quarters filling in twisted bilayer graphene, Science **365**, 605 (2019).

[2] H. Park, J. Cai, E. Anderson, Y. Zhang, J. Zhu, X. Liu, C. Wang, W. Holtzmann, C. Hu, Z. Liu, et al., Observation of fractionally quantized anomalous Hall effect, Nature **622**, 74 (2023).

[3] A. P. Reddy, F. Alsallom, Y. Zhang, T. Devakul, and L. Fu, Fractional quantum anomalous Hall states in twisted bilayer MoTe 2 and WSe 2, Phys. Rev. B **108**, 085117 (2023).

[4] F. Xu, Z. Sun, T. Jia, C. Liu, C. Xu, C. Li, Y. Gu, K. Watanabe, T. Taniguchi, B. Tong, et al., Observation of Integer and Fractional Quantum Anomalous Hall Effects in Twisted Bilayer MoTe 2, Phys. Rev. X **13**, 031037 (2023).

[5] M. Serlin, C. L. Tschirhart, H. Polshyn, Y. Zhang, J. Zhu, K. Watanabe, T. Taniguchi, L. Balents, and A. F. Young, Intrinsic quantized anomalous Hall effect in a moiré heterostructure, Science **367**, 900 (2020).

[6] K. Kang, B. Shen, Y. Qiu, Y. Zeng, Z. Xia, K. Watanabe, T. Taniguchi, J. Shan, and K. F. Mak, Evidence of the fractional quantum spin Hall effect in moiré MoTe2, Nature **628**, 522 (2024).

[7] Y. Cao, V. Fatemi, A. Demir, S. Fang, S. L. Tomarken, J. Y. Luo, J. D. Sanchez-Yamagishi, K. Watanabe, T. Taniguchi, E. Kaxiras, et al., Correlated insulator behaviour at half-filling in magic-angle graphene superlattices, Nature **556**, 80 (2018).

[8] K. P. Nuckolls, M. Oh, D. Wong, B. Lian, K. Watanabe, T. Taniguchi, B. A. Bernevig, and A. Yazdani, Strongly correlated Chern insulators in magic-angle twisted bilayer graphene, Nature **588**, 610 (2020).

[9] S. Wu, Z. Zhang, K. Watanabe, T. Taniguchi, and E. Y. Andrei, Chern insulators, van Hove singularities and topological flat bands in magic-angle twisted bilayer graphene, Nat. Mater. **20**, 488 (2021).

[10] Y. Cao, V. Fatemi, S. Fang, K. Watanabe, T. Taniguchi, E. Kaxiras, and P. Jarillo-Herrero, Unconventional superconductivity in magic-angle graphene superlattices, Nature **556**, 43 (2018).

[11] Y. Saito, J. Ge, K. Watanabe, T. Taniguchi, and A. F. Young, Independent superconductors and correlated insulators in twisted bilayer graphene, Nat. Phys. **16**, 926 (2020).

[12] Z. Zhu, S. Carr, D. Massatt, M. Luskin, and E. Kaxiras, Twisted Trilayer Graphene: A Precisely Tunable Platform for Correlated Electrons, Phys. Rev. Lett. **125**, 116404 (2020).

[13] Z. Hao, A. M. Zimmerman, P. Ledwith, E. Khalaf, D. H. Najafabadi, K. Watanabe, T. Taniguchi, A. Vishwanath, and P. Kim, Electric field–tunable superconductivity in alternating-twist magic-angle trilayer graphene, Science **371**, 1133 (2021).

[14] J. M. Park, Y. Cao, K. Watanabe, T. Taniguchi, and P. Jarillo-Herrero, Tunable strongly coupled superconductivity in magic-angle twisted trilayer graphene, Nature **590**, 249 (2021).

[15] J. Shin, B. L. Chittari, Y. Jang, H. Min, and J. Jung, Nearly flat bands in twisted triple bilayer graphene, Phys. Rev. B **105**, 245124 (2022).

[16] L. Wang, S. Zihlmann, M.-H. Liu, P. Makk, K. Watanabe, T. Taniguchi, A. Baumgartner, and C. Schönenberger, New Generation of Moiré Superlattices in Doubly Aligned hBN/Graphene/hBN Heterostructures, Nano Lett. **19**, 2371 (2019).

[17] A. Uri, S. C. de la Barrera, M. T. Randeria, D. Rodan-Legrain, T. Devakul, P. J. D. Crowley, N. Paul, K. Watanabe, T. Taniguchi, R. Lifshitz, et al., Superconductivity and strong interactions in a tunable moiré quasicrystal, Nature **620**, 762 (2023).

[18] C. Yang, J. May-Mann, Z. Zhu, and T. Devakul, Multi-moiré trilayer graphene: Lattice relaxation, electronic structure, and magic angles, Phys. Rev. B **110**, 115434 (2024).

[19] W. Ren, K. Davydov, Z. Zhu, J. Ma, K. Watanabe, T. Taniguchi, E. Kaxiras, M. Luskin, and K. Wang, Tunable inter-moiré physics in consecutively twisted trilayer graphene, Phys. Rev. B **110**, 115404 (2024).

[20] Z. Zhu, P. Cazeaux, M. Luskin, and E. Kaxiras, Modeling mechanical relaxation in incommensurate trilayer van der Waals heterostructures, Phys. Rev. B **101**, 224107 (2020).

[21] D. Park, C. Park, E. Ko, K. Yananose, R. Engelke, X. Zhang, K. Davydov, M. Green, S. H. Park, J. H. Lee, et al., *Tunable Incommensurability and Spontaneous Symmetry Breaking in the Reconstructed Moir\'e-of-Moir\'e Lattices*, arXiv:2402.15760.

[22] T. Devakul, P. J. Ledwith, L.-Q. Xia, A. Uri, S. C. de la Barrera, P. Jarillo-Herrero, and L. Fu, Magic-angle helical trilayer graphene, Science Advances **9**, eadi6063 (2023).

[23] W. Wang, G. Zhou, W. Lin, Z. Feng, Y. Wang, M. Liang, Z. Zhang, M. Wu, L. Liu, K. Watanabe, et al., Correlated Charge Density Wave Insulators in Chirally Twisted Triple Bilayer Graphene, Phys. Rev. Lett. **132**, 246501 (2024).

[24] L.-Q. Xia, S. C. de la Barrera, A. Uri, A. Sharpe, Y. H. Kwan, Z. Zhu, K. Watanabe, T. Taniguchi, D. Goldhaber-Gordon, L. Fu, et al., *Helical Trilayer Graphene: A Moiré Platform for Strongly-Interacting Topological Bands*, arXiv:2310.12204.

[25] X. Zhang, K.-T. Tsai, Z. Zhu, W. Ren, Y. Luo, S. Carr, M. Luskin, E. Kaxiras, and K. Wang, Correlated Insulating States and Transport Signature of Superconductivity in Twisted Trilayer Graphene Superlattices, Phys. Rev. Lett. **127**, 166802 (2021).

[26] See Supplemental Material at [URL will be inserted by publisher] for more details, which includes Refs. [45-47].

[27] M. V. Berry, Quantal phase factors accompanying adiabatic changes, Proceedings of the Royal Society of London. A. Mathematical and Physical Sciences **392**, 45 (1997).

[28] D. Xiao, M.-C. Chang, and Q. Niu, Berry phase effects on electronic properties, Rev. Mod. Phys. **82**, 1959 (2010).

[29] K. S. Novoselov, E. McCann, S. V. Morozov, V. I. Fal'ko, M. I. Katsnelson, U. Zeitler, D. Jiang, F. Schedin, and A. K. Geim, Unconventional quantum Hall effect and Berry's phase of 2π in bilayer graphene, Nature Phys **2**, 177 (2006).

[30] Y. Shimazaki, M. Yamamoto, I. V. Borzenets, K. Watanabe, T. Taniguchi, and S. Tarucha, Generation and detection of pure valley current by electrically induced Berry curvature in bilayer graphene, Nature Phys **11**, 1032 (2015).

[31] M. Sui, G. Chen, L. Ma, W.-Y. Shan, D. Tian, K. Watanabe, T. Taniguchi, X. Jin, W. Yao, D. Xiao, et al., Gate-tunable topological valley transport in bilayer graphene, Nature Phys **11**, 1027 (2015).

[32] S. Sinha, P. C. Adak, R. S. Surya Kanthi, B. L. Chittari, L. D. V. Sangani, K. Watanabe, T. Taniguchi, J. Jung, and M. M. Deshmukh, Bulk valley transport and Berry curvature spreading at the edge of flat bands, Nat Commun **11**, 5548 (2020).

[33] E. Arrighi, V.-H. Nguyen, M. Di Luca, G. Maffione, Y. Hong, L. Farrar, K. Watanabe, T. Taniguchi, D. Mailly, J.-C. Charlier, et al., Non-identical moiré twins in bilayer graphene, Nat Commun **14**, 8178 (2023).

[34] C. Ma, Q. Wang, S. Mills, X. Chen, B. Deng, S. Yuan, C. Li, K. Watanabe, T. Taniguchi, X. Du, et al., Moiré Band Topology in Twisted Bilayer Graphene, Nano Lett. **20**, 6076 (2020).

[35] R. V. Gorbachev, J. C. W. Song, G. L. Yu, A. V. Kretinin, F. Withers, Y. Cao, A. Mishchenko, I. V. Grigorieva, K. S. Novoselov, L. S. Levitov, et al., Detecting topological currents in graphene superlattices, Science **346**, 448 (2014).

[36] K. Komatsu, Y. Morita, E. Watanabe, D. Tsuya, K. Watanabe, T. Taniguchi, and S. Moriyama, Observation of the quantum valley Hall state in

ballistic graphene superlattices, Science Advances **4**, eaaq0194 (2018).

[37] Y. Li, M. Amado, T. Hyart, G. P. Mazur, and J. W. A. Robinson, Topological valley currents via ballistic edge modes in graphene superlattices near the primary Dirac point, Commun Phys **3**, 1 (2020).

[38] K. Endo, K. Komatsu, T. Iwasaki, E. Watanabe, D. Tsuya, K. Watanabe, T. Taniguchi, Y. Noguchi, Y. Wakayama, Y. Morita, et al., Topological valley currents in bilayer graphene/hexagonal boron nitride superlattices, Applied Physics Letters **114**, 243105 (2019).

[39] D. A. Abanin, S. V. Morozov, L. A. Ponomarenko, R. V. Gorbachev, A. S. Mayorov, M. I. Katsnelson, K. Watanabe, T. Taniguchi, K. S. Novoselov, L. S. Levitov, et al., Giant Nonlocality Near the Dirac Point in Graphene, Science **332**, 328 (2011).

[40] J. Salvador-Sánchez, L. M. Canonico, A. Pérez-Rodríguez, T. P. Cysne, Y. Baba, V. Clericò, M. Vila, D. Vaquero, J. A. Delgado-Notario, J. M. Caridad, et al., Generation and control of nonlocal chiral currents in graphene superlattices by orbital Hall effect, Phys. Rev. Res. **6**, 023212 (2024).

[41] Z. Wu, B. T. Zhou, X. Cai, P. Cheung, G.-B. Liu, M. Huang, J. Lin, T. Han, L. An, Y. Wang, et al., Intrinsic valley Hall transport in atomically thin MoS2, Nat Commun **10**, 611 (2019).

[42] M. Beconcini, F. Taddei, and M. Polini, Nonlocal topological valley transport at large valley Hall angles, Phys. Rev. B **94**, 121408 (2016).

[43] J. Liu, Z. Ma, J. Gao, and X. Dai, Quantum Valley Hall Effect, Orbital Magnetism, and Anomalous Hall Effect in Twisted Multilayer Graphene Systems, Phys. Rev. X **9**, 031021 (2019).

[44] Konstantin Davydov, Ziyan Zhu, Noah Friedman, Ethan Gramowski, Yaotian Li, Jack Tavakley, Kenji Watanabe, Takashi Taniguchi, Mitchell Luskin, Efthimios Kaxiras, et al., 2025, Zenodo, 10.5281/zenodo.15110600.

[45] M. Koshino, Band structure and topological properties of twisted double bilayer graphene, Phys. Rev. B **99**, 235406 (2019).

[46] C. R. Dean, A. F. Young, I. Meric, C. Lee, L. Wang, S. Sorgenfrei, K. Watanabe, T. Taniguchi, P. Kim, K. L. Shepard, et al., Boron nitride substrates for high-quality graphene electronics, Nature Nanotech **5**, 10 (2010).

[47] L. Wang, I. Meric, P. Y. Huang, Q. Gao, Y. Gao, H. Tran, T. Taniguchi, K. Watanabe, L. M. Campos, D. A. Muller, et al., One-Dimensional Electrical Contact to a Two-Dimensional Material, Science **342**, 614 (2013).

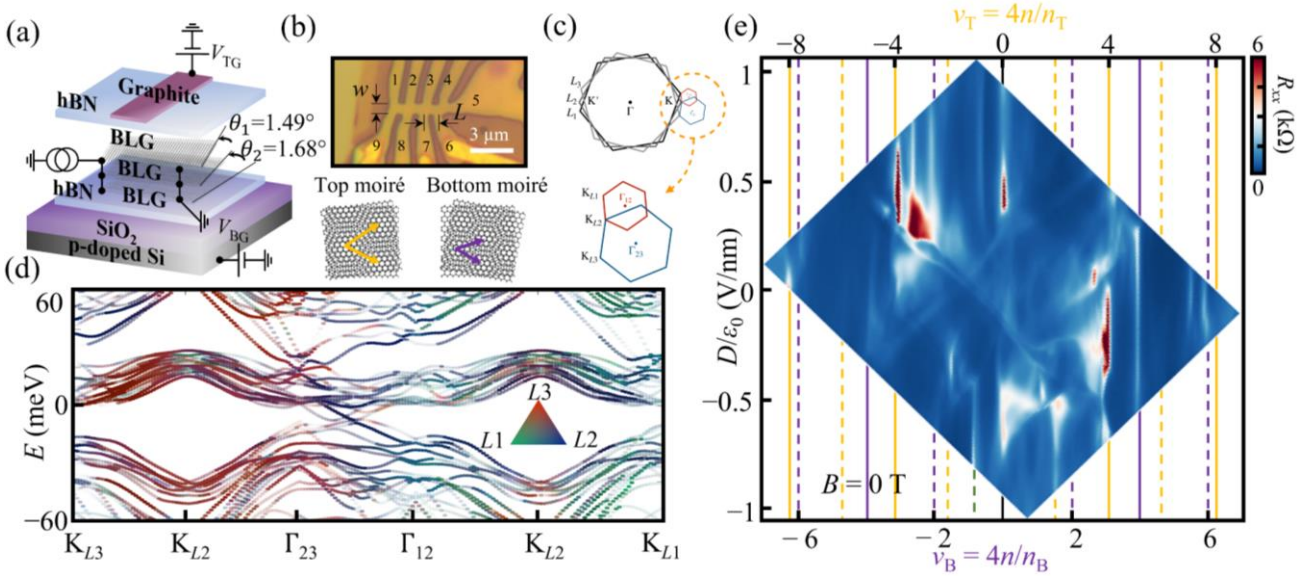


FIG. 1. Gate-tunable insulating states of competing moiré superlattices in tTBLG. (a) Schematic architecture of the dual gated (with applied top, V_{TG}, and back, V_{BG}, gate voltages) tTBLG stack with the two consecutive twist angles of 1.49° and 1.68° measured under applied current bias. (b) Upper: optical micrograph of the Hall bar shaped tTBLG device with L and w being the length and width of the channel. Lower: schematic images of the coexisting top (bottom) moiré superlattices, with the yellow (purple) arrows indicating the corresponding unequal superlattice vectors. (c) Top: the relative position of the Brillouin zones of each of the three BLGs. Bottom: the alignment of the two mini-Brillouin zones of different sizes corresponding to the top and bottom moirés. (d) Calculated band structure of tTBLG at the twist angles of 1.49° and 1.68° along high symmetry points of the mini-Brillouin zones. Colors indicate the projected weight of each BLG layer. Top layer: green; middle layer: blue; bottom layer: red. (e) The measured four-probe longitudinal resistance R_{xx} as a function of the top (bottom) moiré filling factors and displacement field, D. Displacement field asymmetric insulating states are observed at full (solid lines) and half (dashed lines) fillings of the two moiré superlattices.

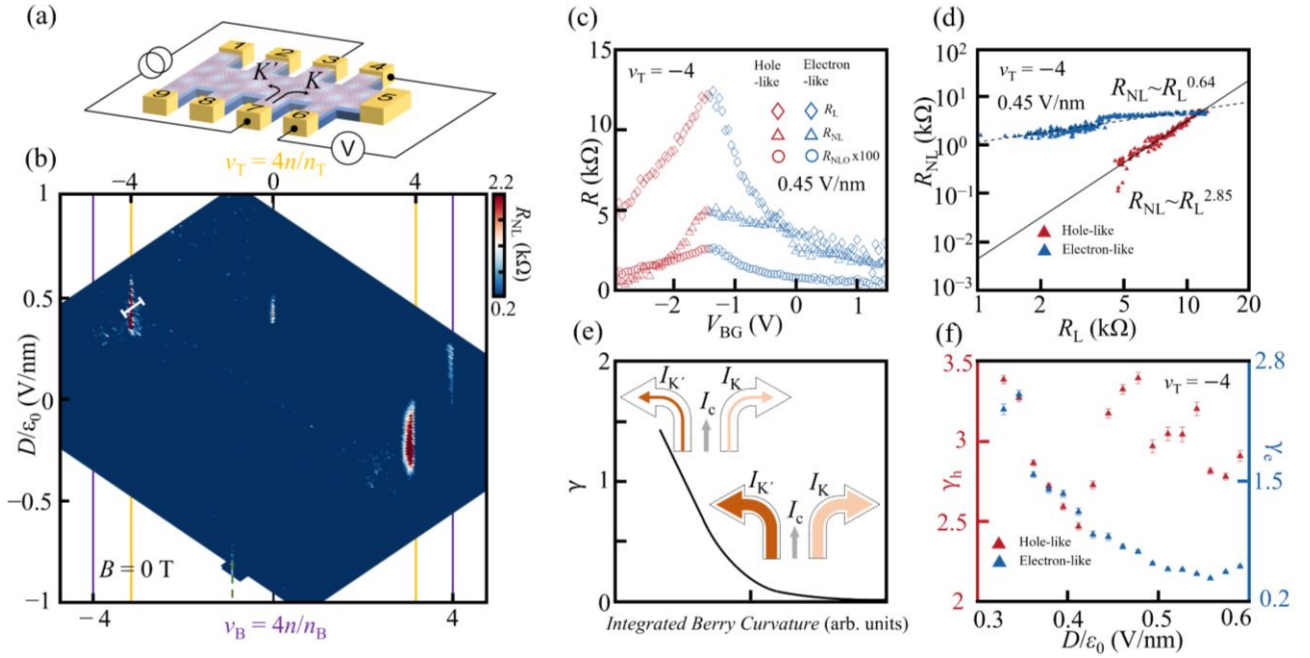


FIG. 2. Atomic lattice reconstruction enhanced moiré Berry curvature hot spot. (a) Nonlocal signal measurement configuration with currents from the different valleys bending in the opposite directions resulting in a transverse valley current. (b) Measured nonlocal resistance $R_{NL} = V_{64}/I_{73}$ (ratio between the measured nonlocal voltage and driven current) as a function of D and n. Five peaks are visible corresponding to different Berry curvature hot spots. The white bar represents the horizontal range of the resistance cuts in Fig. 2(c). (c) Nonlocal (R_{NL}), local (R_L), and nonlocal Ohmic (R_{NLO}) resistances due to the stray charge currents near $\nu_T = -4$ and at $D/\varepsilon_0 = +0.45$ V/nm. (d) R_{NL} versus R_L for hole-like (red) and electron-like (blue) carriers near $\nu_T = -4$ at $D/\varepsilon_0 = +0.45$ V/nm. The solid and dashed lines correspond to power law fits for the hole- and electron-like carriers. (e) Qualitative evolution of the power law dependence $R_{NL} \sim R_L^{\gamma}$ as a function of magnitude of the integrated Berry curvature. The inset shows the change in the relative magnitudes of the charge (I_c) and the corresponding valley currents (I_K, $I_{K'}$) as the Berry curvature (and thus, the ratio between the valley Hall and charge conductance) increases. (f) Displacement field dependence of the powers of the $R_{NL} \sim R_L^{\gamma_h}$ ($R_{NL} \sim R_L^{\gamma_e}$) laws for the hole- (electron-) like charge carriers.

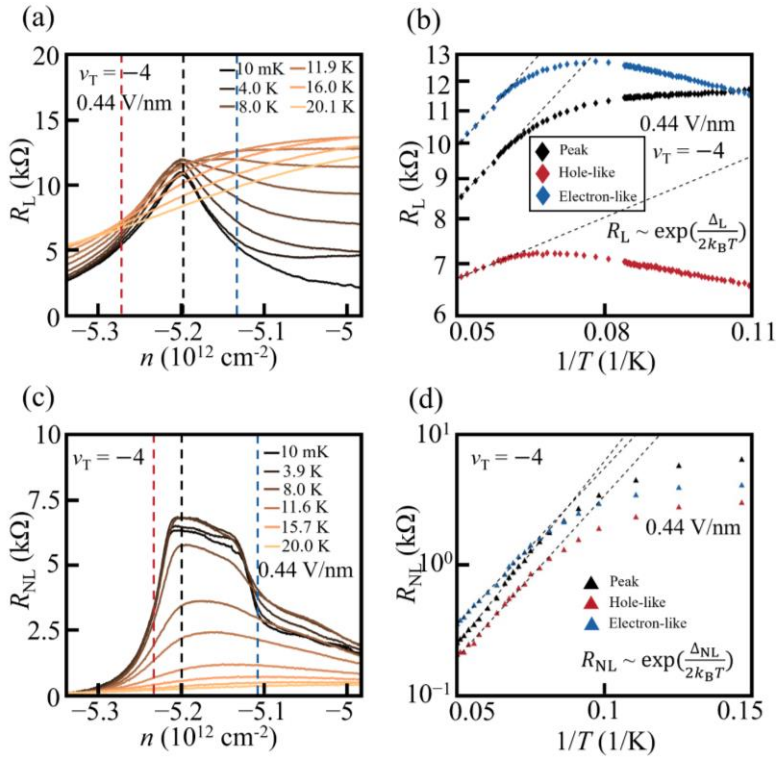


FIG. 3. Temperature dependences of local and nonlocal resistance near moiré Berry curvature hot spot. (a) Thermal activation behavior of R_L near $\nu_T = -4$ at $D/\varepsilon_0 = +0.44$ V/nm. The black dashed line indicates the position of the peak resistance at 10 mK; the blue and red dashed lines trace R_L at half the peak height at 10 mK for the electron- and hole-like charge carriers respectively. Each curve corresponds to a selected temperature increasing from 10 mK to 20 K (indicated by the color) with an increment of $\Delta T \sim 2$ K. (b) Local resistance (black: peak; red: hole-like half-peak; blue: electron-like half-peak) of the $\nu_T = -4$ BI state as a function of inverse temperature $1/T$ at $D/\varepsilon_0 = 0.44$ V/nm. The dashed lines indicate Arrhenius fits of the resistance with thermally activated behavior regime. (c) Same as (a) but for R_{NL} near $\nu_T = -4$ at $D/\varepsilon_0 = +0.44$ V/nm. Similar to (a), the dashed lines indicate R_{NL} at the peak (black) and half-peak (red, blue matching the carrier type) of the resistance curve at 10 mK. Each curve is taken at a different temperature rising from 10mK to 20K with a step of $\Delta T \sim 2$ K. (d) Temperature dependence of the peak (black) and half peak R_{NL} for the electron-like (blue) and hole-like (red) carriers. The dashed lines represent Arrhenius fits at $T > 10$ K.

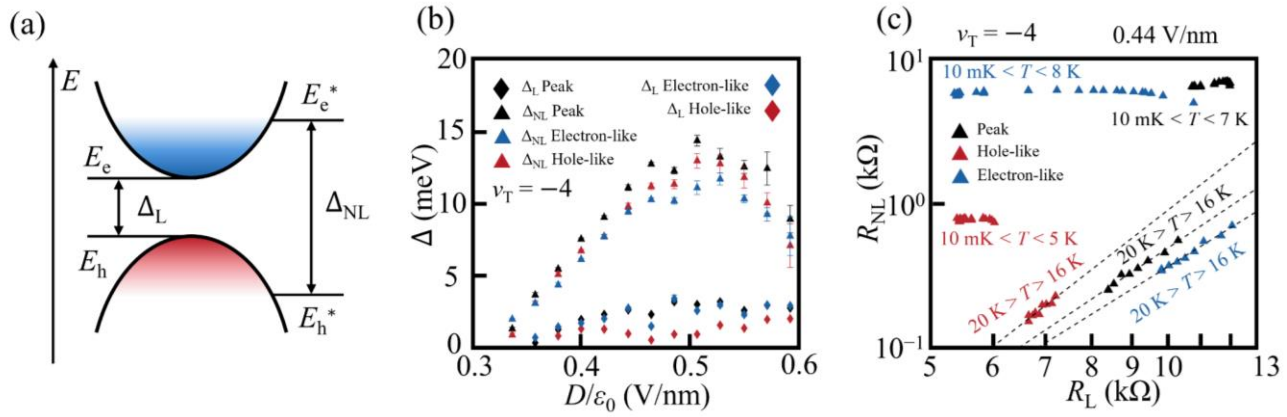


FIG. 4. Characteristic energies of moiré Berry curvature hot spot. (a) Illustration of different energy scales of a moiré Berry curvature hot spot. The local band gap Δ_L matches the band insulator gap and equals the difference between the conduction and valence band edges energies E_e, and E_h. The size of the nonlocal band gap $\Delta_{NL} = E_e^* - E_h^*$ determined by the energies $E_e^*(E_h^*)$ above (below) which the Berry curvature labeled by blue (red) vanishes in the electron- (hole-) band. (b) The size of the local (Δ_L) and nonlocal (Δ_{NL}) band gaps found from the Arrhenius fits of the peak (black) and half peak (blue and red, matching the carrier type) value of the resistance as a function of D. (c) Log-log plot of R_{NL} (nonlocal resistance) dependence on R_L (local resistance) for electron-like (blue) doping, hole-like (red) doping, and in-gap (black) near $\nu_T = -4$ BI at $D/\varepsilon_0 = +0.44$ V/nm. Data points are taken at varying temperatures. At low temperature range below T ~10 K, the ballistic valley conduction channel is saturated, and thermally activated additional carriers are capable of contributing to local transport only. R_{NL} remains constant while R_L is rapidly decreasing with T, resulting in power law of $\gamma < 0.5$. At higher temperature ($T > 10$ K), charge carriers are thermally excited away from Berry curvature hot spot. The weaker Berry curvature makes the ballistic valley conducting channel unsaturated, resulting in an observed power law of $\gamma > 3$.